SUPPORTING INFORMATION

Fate of Plutonium at a Former Nuclear Testing Site in Australia

Atsushi Ikeda-Ohno,*[1,2,3] Lida Mokhber Shahin,[2] Daryl L. Howard,[4] Richard N. Collins,[3] Timothy E. Payne[2] and Mathew P. Johansen*[2]

[1] Helmholtz-Zentrum Dresden-Rossendorf, Institute of Resource Ecology, Bautzner Landstrasse 400, 01328 Dresden, Germany.

[2] Institute for Environmental Research, Australian Nuclear Science and Technology Organisation, Locked Bag 2001, Kirrawee DC, New South Wales 2232, Australia.

[3] School of Civil and Environmental Engineering, the University of New South Wales, Sydney, New South Wales 2052, Australia.

[4] Australian Synchrotron, 800 Blackburn Road, Clayton, Victoria 3168, Australia.

*Correspondence to a.ikeda@hzdr.de (A.I.-O.) or mjo@ansto.gov.au (M.P.J.)

Contents

Experimental **3**

Site background

Gamma-ray spectrometry

X-ray fluorescence microscopy / X-ray absorption spectroscopy

Supplementary discussion **6**

Elemental distribution of Pu “hot” particle

X-ray absorption spectroscopy at Pu L_{III}-edge

Morphology of the isolated Pu particle

References **18**

Experimental

Site Background

From 1961–63, approximately 22 kg of plutonium (Pu) were used in twelve "*Safety Trials*" (or "*Minor Trials*"), so-called the "*Vixen B*" series, conducted at the Taranaki test site in Maralinga, South Australia (Fig. 1-(c) in the main text). In these tests, various components of nuclear devices were subjected to a range of explosive and burning conditions designed to simulate non-fission, or partial-fission accidents involving nuclear weapons.[1] The resulting dispersal of material was energetic with Pu-containing particles of submicron to >150 μm diameter sizes deposited in down-wind surface contamination plumes, some of which extend more than 25 km.[2] Although areas near the firing pad were subsequently remediated (in the 1960s and in the late 1990s), most of the deposition plume areas have remained undisturbed for more than fifty years since the original dispersal, during which the particles have been subjected to semi-arid environmental conditions (mean annual rainfall of 200 mm, monthly mean temperatures ranging from 13–25 °C with summer daytime temperatures exceeding 40 °C).[1]

Gamma-ray spectrometry

As described in the main text, the collected soils were processed to eventually obtain a single "hot" particle representing the majority of the detected activity in the original soils. The isolated particle was found to be highly friable and easily fragmented into smaller pieces when pressed on a glass slides (Figure S1). The isolated particle was analysed with gamma-ray spectrometry in order to find possible co-existing radionuclides in the particle. Figure S2 shows the gamma-ray spectrum of the isolated particle. Only one significant peak was observed at around 60 keV, which is attributed to the gamma radiation of ^{241}Am (59.54 keV). No significant contribution of fission products (FPs) was detected as there was no other measurable radionuclide peak present in the spectrum (Figure S2), for instance the ^{137}Cs peak at 661.66 keV was below detection limit. This is a clear indication that the original material of the isolated particle did not undergo fission reactions when detonated and, hence, it originates in "*Minor Trials*", not tests involving nuclear detonation (i.e., "*Major Trials*").[1, 3]

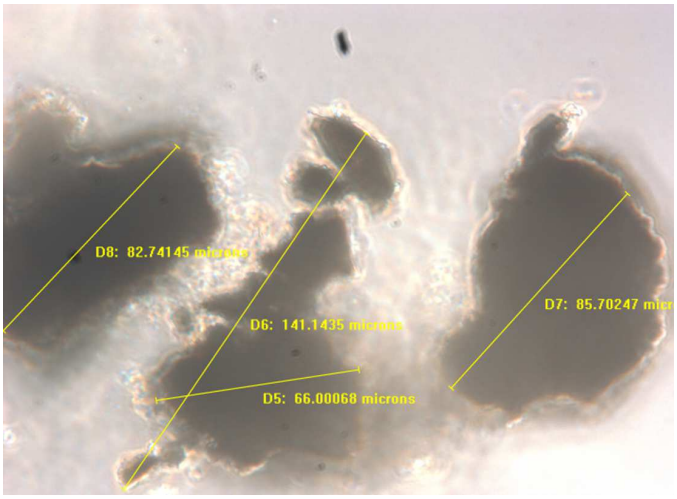

Figure S1. Optical microscope image of the isolated particle exhibiting high ^{241}Am activity.

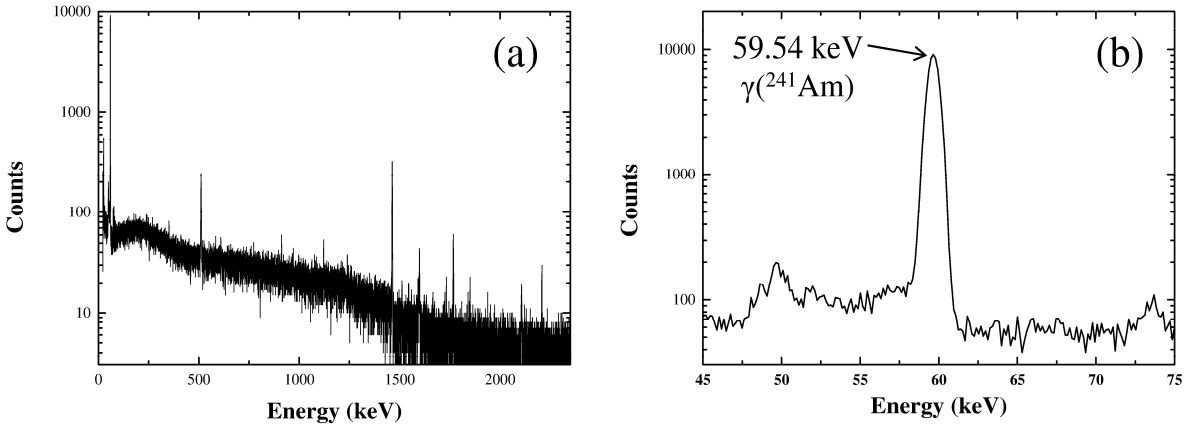

Figure S2. Total gamma-ray spectrum of the isolated particle (a) and its enlargement on the lower energy region (b). Measurement duration; 65725 sec.

X-ray fluorescence microscopy / X-ray absorption spectroscopy

XFM measurements were performed at the XFM beamline[4] of the Australian Synchrotron under ring operating conditions of 3 GeV and 200 mA with top-up mode. Scanning X-ray fluorescence (XRF) mapping[5] and X-ray absorption near edge structure (XANES) mapping in fluorescence mode[6] at the Pu L_{III}-edge (18.057 keV) were carried out under ambient conditions with a Kirkpatrick-Baez (KB) mirror pair and the Maia detector.[7] XANES mapping produces a XANES spectrum from the X-ray fluorescence signal at selected pixels in a stack of images collected as a function of incident beam energy. For XANES mapping measurements, X-ray absorption spectra of Zr foil was acquired simultaneously in transmission mode for energy calibration (at the Zr K-edge, defined as 17999.35 eV at the 1st inflection point) upstream of the KB mirrors. The acquired data were treated and analysed with the software GeoPIXE (Version 6.6)[8] and WinXAS (Version 3.2).[9] The acquired X-ray

fluorescence data were deconvoluted based on the Dynamic Analysis matrix transform method[10] to obtain elemental concentration maps as a function of incident beam energy. Pu L_{III}-edge X-ray absorption spectra were produced based on the total counts of the observed Pu L fluorescence lines (Figs. S3 and S4) on a selected region covering the whole area of each sample fragment. The data treatment for the extended X-ray absorption fine structure (EXAFS) region was performed with the software WinXAS[9] according to the standard procedure.[11] Theoretical phase and amplitude for EXAFS theoretical fitting were calculated by a program code FEFF8.20[12] based on the crystal structures of metallic Pu and PuO_2.[13]

As synchrotron radiation is obviously an extremely intensive X-ray source, radiation damage on the samples would be a potential issue of synchrotron-based X-ray experiments. In order to consider potential radiation damage on our samples during the measurement, we would first consider our experiences at the beamline BM20 (ROBL), ESRF.[14] The beamline BM20 is a special beamline dedicated to the synchrotron measurements with radioactive samples and equipped with a bending magnet source, generating the photon flux of approximately 6×10^{11} photons/sec on a focused beam spot of 0.5×0.5 mm^2 at 20 keV. Assuming one hour of measurement time (typical measurement time for a single scan to collect a whole range of X-ray absorption spectrum at actinide L-edges), the sample will be exposed to $\sim 2 \times 10^{15}$ photons for a single scan. Under this radiation conditions, no significant radiation damage has been reported on the publication from the relevant beamline (e.g., *via* the publication database of the beamline BM20 on ResearcherID under; http://www.researcherid.com/rid/A-2586-2011). There are a small number of examples reporting radiation damage on the samples measured at BM20. These samples are, however, all solution samples, in which the radiation damage on the target metal species is caused indirectly *via* the interaction with the solvent molecules radicalised by synchrotron radiation. Hence, this indirect radiation damage is not expected for solid samples.

In our XFM measurements on our Pu solid samples at the Australian Synchrotron, the longest exposure time on a single spot on the sample was 76 sec (0.03125 sec dwell per 2 micron pixel of spot with 243 energy points for XANES scanning). The calculated photon flux at the XFM beamline is 7×10^8 photons/sec at Pu L_{III}-edge (17.610 keV). Hence, the most intensive radiation on a single spot of our Pu samples is estimated to be $\sim 5 \times 10^{10}$ photons, which is five orders of magnitude weaker than the radiation estimated at the beamline BM20 (2×10^{15} photons). Given all these facts, we conclude that there was no significant radiation damage on our Pu samples during the XFM measurements and the obtained results are reliable.

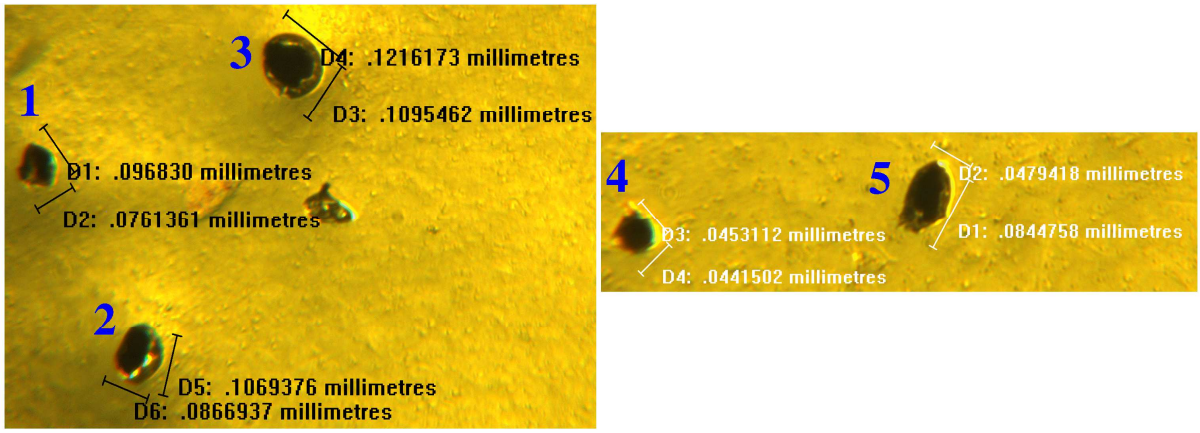

Figure S3. Optical microscope images of five fragments of the isolated particle exhibiting high ^{241}Am activity with dimension information (in millimetres). Significant intensity of Pu fluorescence was detected on all the fragments. The X-ray fluorescence spectrum collected on the fragment **3** is given in Figure S4.

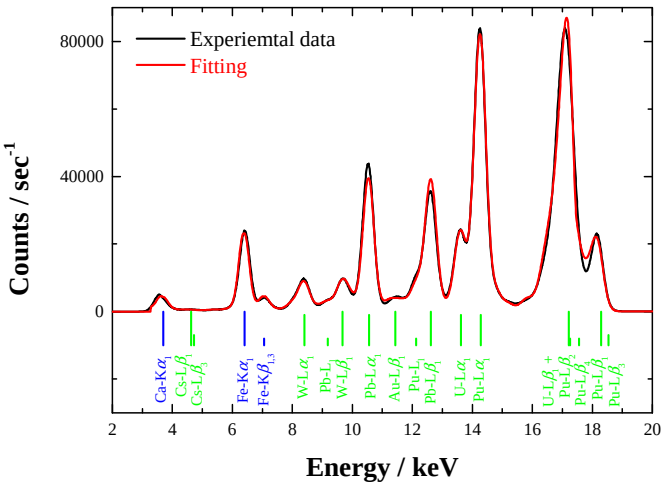

Figure S4. X-ray fluorescence spectrum of the largest fragment (the fragment **3** in Figure S3) of the isolated particle, showing fluorescence signals from Pu L-lines with additional contribution from Ca K-, Fe K-, W L-, Au L-, Pb L- and U L-lines. The incident X-ray energy, 18.167 keV, excites a sufficient range of elements in the isolated particle. The most intense peak at around 17 keV corresponds to the Compton scattering.

Supplementary discussion

Elemental distribution of Pu "hot" particle

Figure S5 shows the X-ray fluorescence spectra of the measured fragments (i.e., the fragments **1**, **2**, **4** and **5** in Figure S3). The fluorescence spectrum for the fragment **3** was already given in Figure S4. A significant intensity of Pu fluorescence was detected on all the fragments. All the fragments show similar X-ray fluorescence spectra which are composed of Ca K-, Fe K-, W L-, Au L-, Pb L- and U L-

and Pu L-lines, being consistent with their common origin from a single particle. The observed similarity in the X-ray fluorescence spectra therefore indicates that the detected elements are common to the original particle. The presence of W in the fragments results from the density separation process using LST (polytungstate) and it is a surface expression. Similarly, the Au results from a fine Au-plated needle used for sample mounting. In fact, the Au is not present within the particle (e.g., Figure S8), but it primarily reflects small residuals stuck on the Kapton tape around the Pu particles.

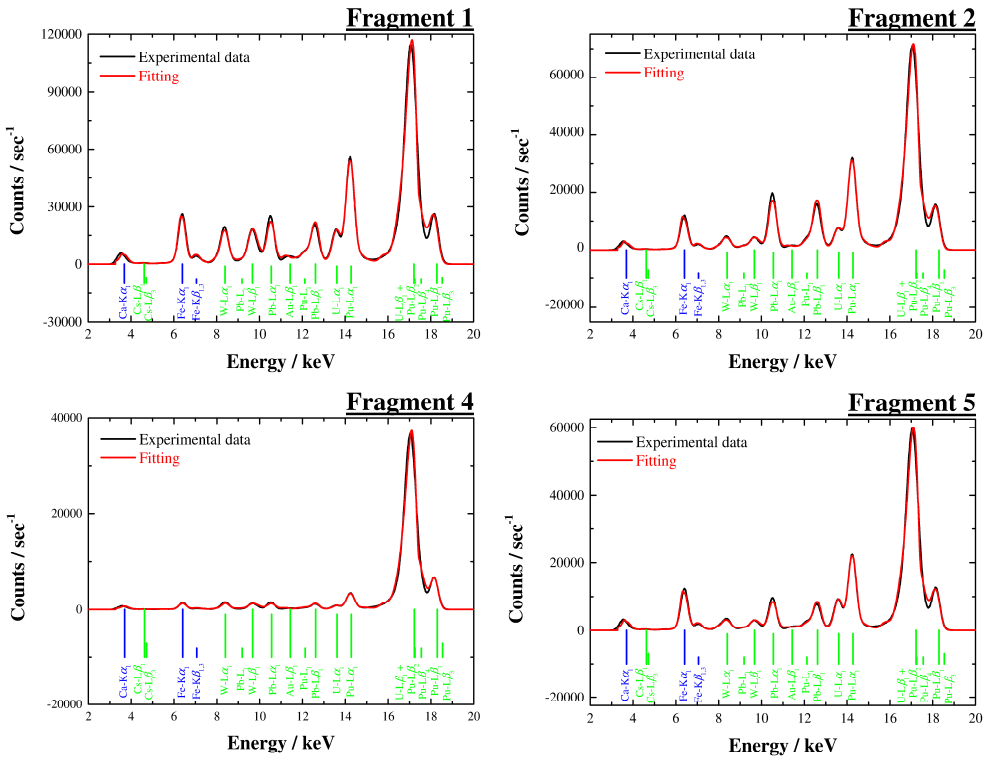

Figure S5. X-ray fluorescence spectra of the fragments **1**, **2**, **4** and **5** in Figure S2. The incident X-ray energy = 18.167 keV. The most intense peak at around 17 keV corresponds to the Compton scattering.

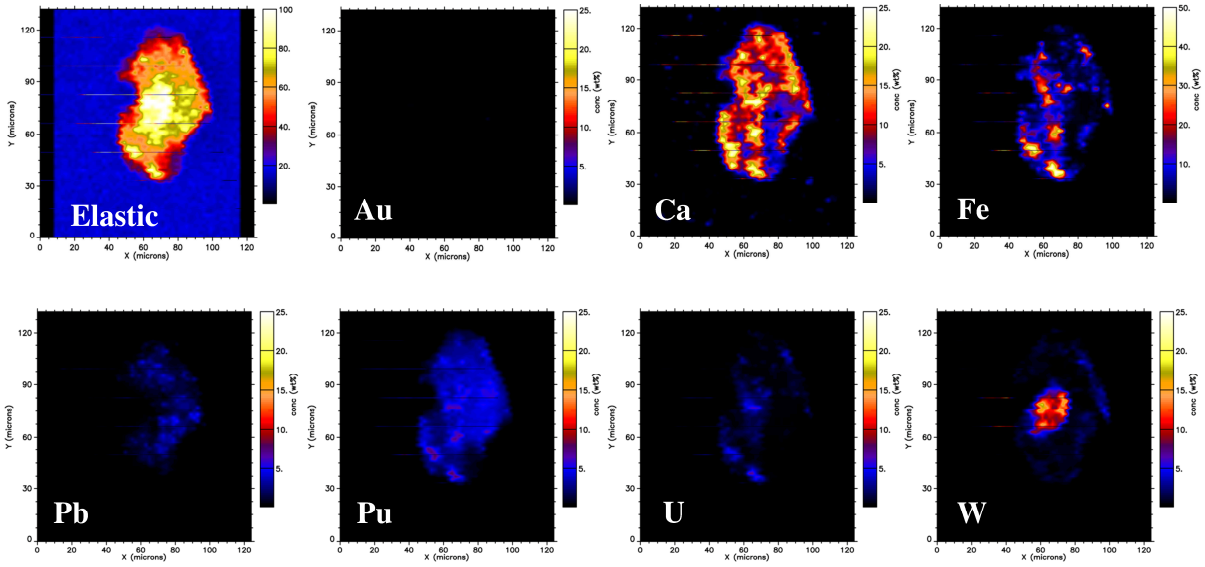

Figure S6. XFM images of the fragment **1** in Figure S3. Incident X-ray energy = 18.070 keV.

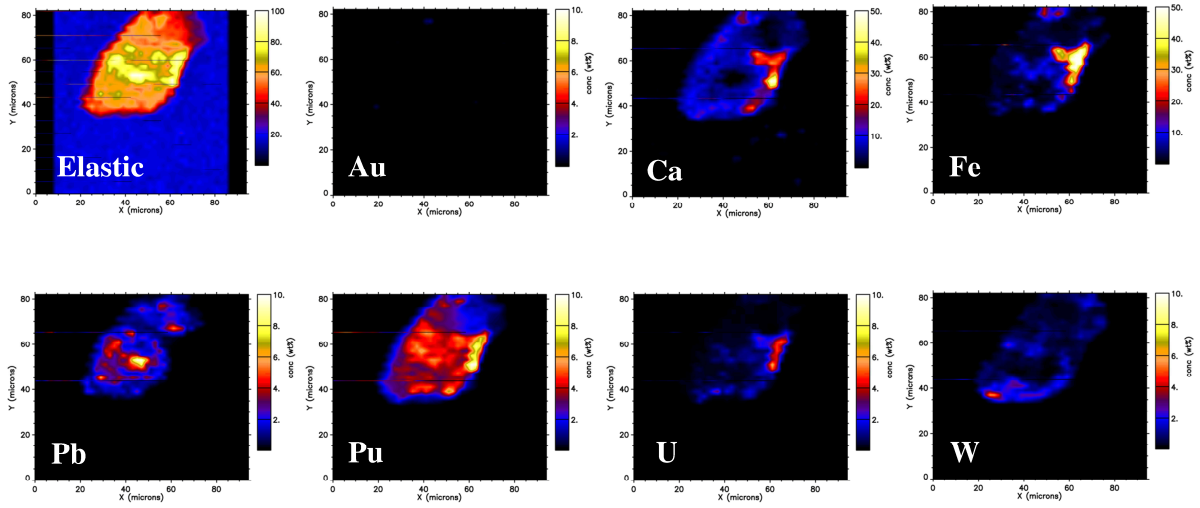

Figure S7. XFM images of the fragment **2** in Figure S3. Incident X-ray energy = 18.070 keV.

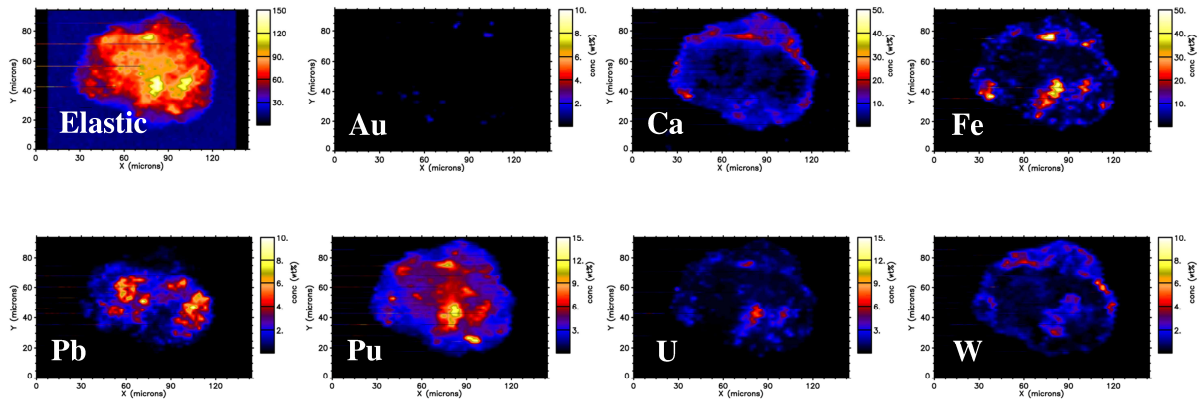

Figure S8. XFM images of the fragment **3** in Figure S3. Incident X-ray energy = 18.070 keV. Due to the data treatment and visualisation process, the images are provided as mirror images of those shown in Figure 2.

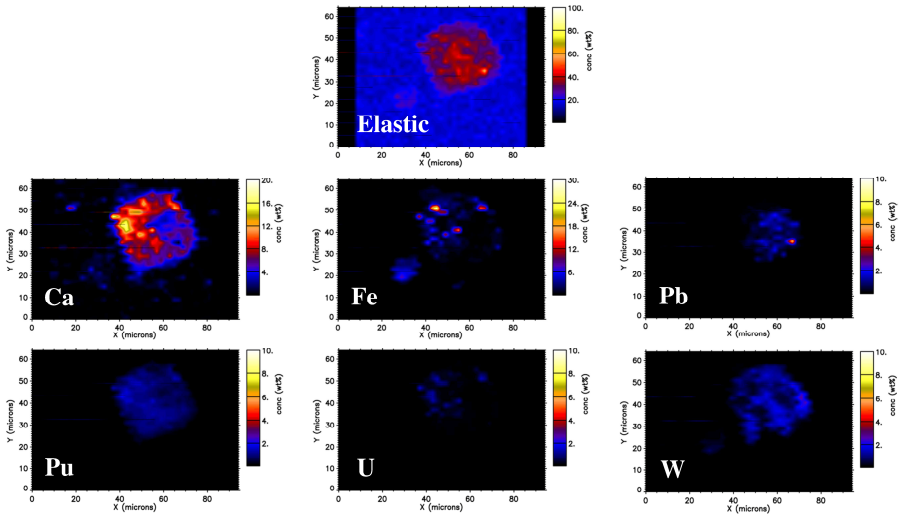

Figure S9. XFM images of the fragment **4** in Figure S3. Incident X-ray energy = 18.070 keV. No significant contribution of Au was detected on the fragment.

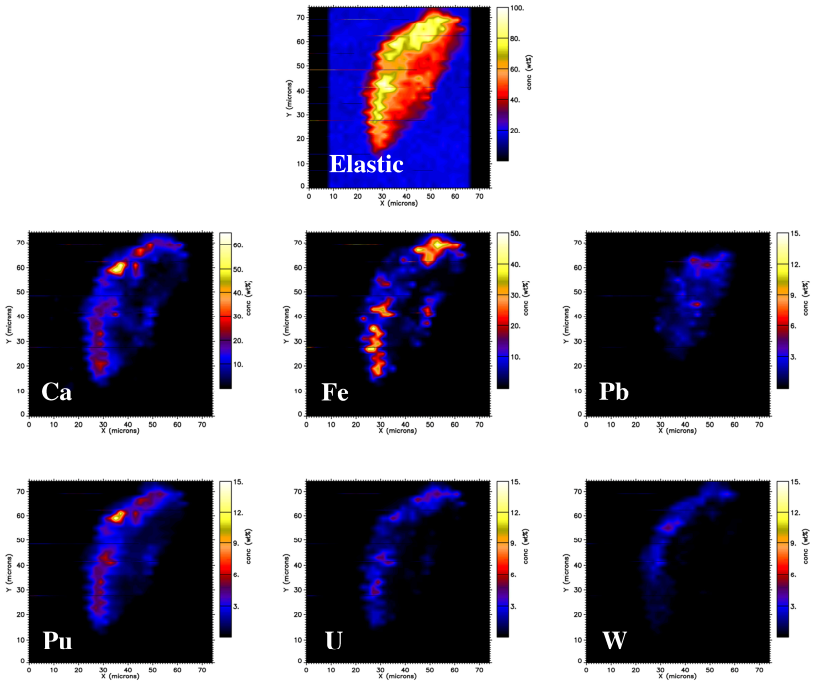

Figure S10. XFM images of the fragment **5** in Figure S3. Incident X-ray energy = 18.070 keV. No significant contribution of Au was detected on the fragment.

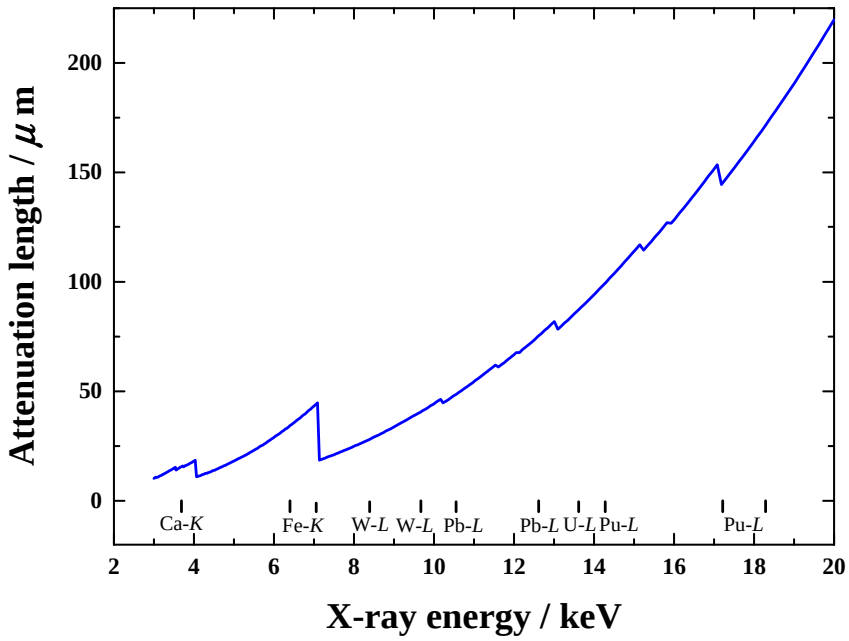

Figure S11. Attenuation length (λ) of X-rays in the isolated particle. The λ value is defined as the depth into the material where the intensity of the X-rays has decreased to about 37% (1/*e*) of the value at the surface. The chemical composition of the particle was estimated as "$Ca_{0.363}Fe_{0.571}W_{0.016}Pb_{0.014}U_{0.012}Pu_{0.024}$" based on the elemental concentrations obtained for the fragment **3** by XRF mapping. The calculation was performed by using the code "*X-ray Attenuation Length*".[15]

X-ray absorption spectroscopy at Pu L_{III}-edge

In general, an X-ray absorption spectrum can be divided into two regions; X-ray absorption near-edge structure (XANES) observed in the region of several tens of eV around the absorption edge, and extended X-ray absorption fine structure (EXAFS) which is extended in a higher energy region with fine oscillation structure above the absorption edge. The former corresponds to the excitation of core electrons to unoccupied orbitals and/or valence bands and, hence, it primarily reflects the electronic structure of the excited atom, such as oxidation states. On the other hand, the EXAFS region derives from the interaction of the photoelectrons released from the atomic centre with the surrounding atoms, reflecting the local structural arrangement around the excited atom.

Figure S12 shows the Pu L_{III}-edge XANES spectra for all the fragments along with reference compounds of metallic Pu ($Pu_{0.965}Ga_{0.035}$) [16] and PuO_2.[17] The energy of the absorption edge (defined as the first inflection point) and XANES peak position is also summarised in Figure S13. The absorption

edge of all the fragments ranges from 18.061 to 18.062 keV, corresponding to those for Pu(IV) solid compounds (red plots in Figure S13). All the fragments show clear XANES peaks at around 18.070 keV (Figure S12) which is much higher than that for metallic Pu (18.067 keV) but comparable with Pu(IV) compounds (Figure S13). As discussed in the main text, the initial Pu component was subject to several oxidative environments upon the explosion and for more than fifty years of local weathering. Therefore, the XANES spectra of the fragments can be interpreted as oxides and/or oxyhydroxide compounds (i.e., $PuO_{2+x-y}(OH)_{2y}\cdot zH_2O$).[16, 18] Conradson *et al.* reported that the XANES peak positions of the Pu oxyhydroxide compounds prepared at temperatures of up to 1,000 ^{o}C exhibit a high-energy shift as compared with that for pure PuO_2.[16] The Pu fragment samples also show a similar high-energy shift in the XANES peak positions as compared with pure PuO_2 (Figure S12). This would be consistent with the temperatures expected during the testing at Taranaki, where the original Pu fuel component underwent detonation-explosion events producing sufficient energy to propel fragments high into the air resulting in deposition plumes of more than 25 km in length.[1] Therefore, it is reasonable to consider that the core of the Pu particle is generated *via* a high-temperature reaction of the Pu fuel component upon the initial detonation-explosion process. The Ca/Fe/U layer on the particle surface is consistent with expected reactions with soil and soil water following rainfall over the decades subsequent to the deposition of the initial Pu particles.

The oxidation of Pu metal could also generate Pu_2O_3.[18] However, this Pu_2O_3 phase is eventually oxidised to PuO_2 in the presence of oxygen (i.e., under atmospheric conditions).[18] The formation of other lower oxides (e.g., PuO) is very unlikely.[19] Hence, based on the XANES data, it is reasonable to deduce that Pu in the particle is primarily in the tetravalent form (Pu(IV)) as oxide and/or oxyhydroxide compounds.

The right figure in Figure S14 shows the normalised Pu L_{III}-edge XANES spectra obtained from different regions of interest (ROI) on the XFM image of the fragment **3**. All the obtained spectra show similar shapes with similar XANES edge and peak positions, suggesting that the Pu species in the fragment are chemically homogeneous.

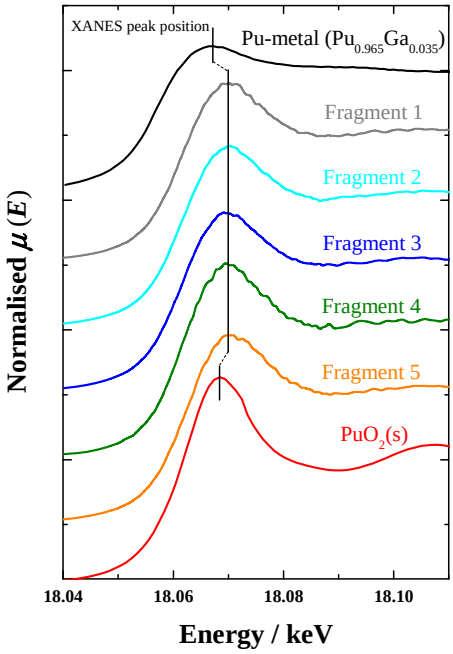

Figure S12. Normalised Pu L_{III}-edge XANES spectra for the fragments of the isolated particle along with reference compounds of metallic Pu ($Pu_{0.965}Ga_{0.035}$) and PuO_2. The spectra for $Pu_{0.965}Ga_{0.035}$[16] and PuO_2[17] were provided through the courtesy of S. D. Conradson (Los Alamos National Lab) and P. M. Martin (CEA-Cadarache), respectively.

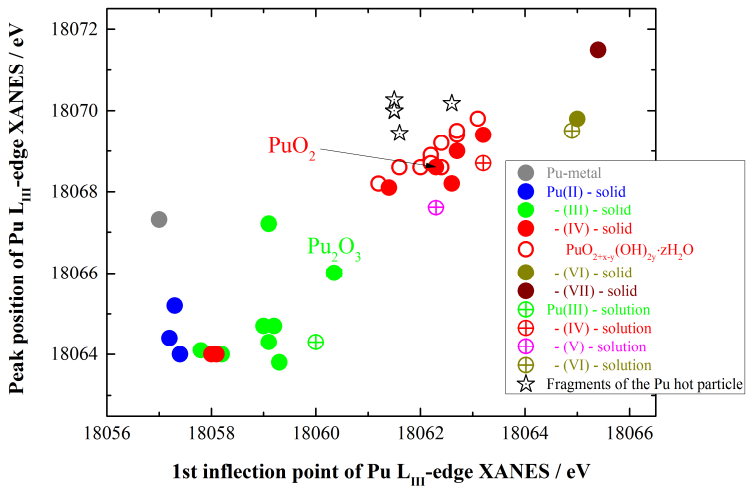

Figure S13. Correlation between the first inflection point (*x*-axis) and peak position (*y*-axis) of Pu L_{III}-edge XANES spectra for the fragments of the isolated particle (black star data) along with those reported for aqueous Pu species and solid Pu compounds with different oxidation states.[16, 20] The energy of the data was corrected according to the first inflection point of Zr foil (defined as 17999.35 eV).

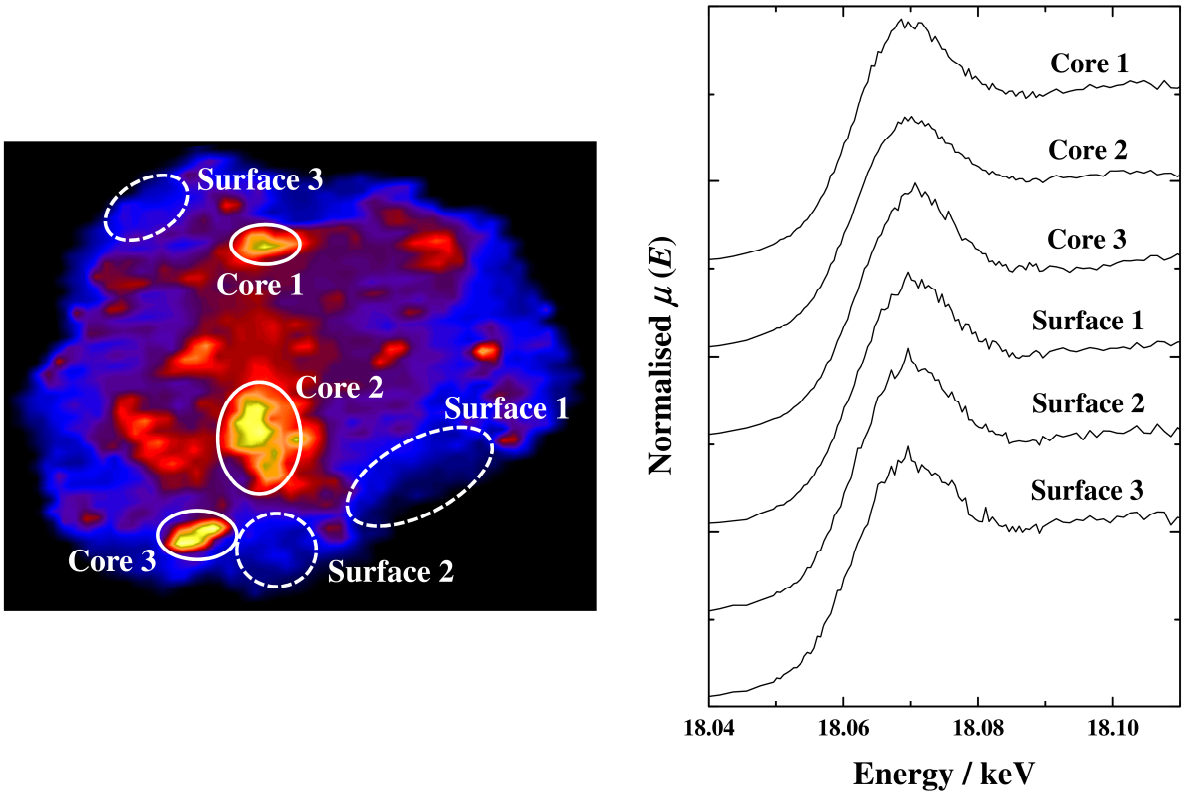

Figure S14. (left) XFM image of Pu distribution on the fragment **3** in Figure S3 and regions of interest (ROI, white circles) used to extract Pu LIII-edge XANES spectra. (right) Normalised Pu L_{III}-edge XANES spectra obtained from the ROI defined on the left figure. The energy of the data in the right figure was corrected according to the first inflection point of Zr foil (defined as 17999.35 eV).

In order to further identify the chemical form of Pu in the particle, the EXAFS region of the X-ray absorption spectra was analysed. Five X-ray absorption spectra collected for the five fragmented samples (the fragments **1**-**5** in Figure S3) were averaged to obtain a single X-ray absorption spectrum, assuming that there is little difference in the chemical form of Pu among the five fragments. This assumption is reasonable in light of the fact that all the five fragments originate from the single particle.

Shown in Figure S15 are the k^3-weighted Pu L_{III}-edge EXAFS spectrum (left) and their corresponding Fourier transform (FT, right) for the Pu particle (blue data, the averaged data of the five fragment samples) together with those of a reference compound of PuO_2(s) (red data).[17] EXAFS metrical parameters obtained from theoretical curve fitting are summarised in Table S1. It has been deduced from the XANES data that the Pu in the particle is likely to be the oxide and/or oxyhydroxide form of Pu(IV). Owing to the similarity of local structure around the Pu centre, the oxyhydroxide compounds of Pu(IV) often show EXAFS oscillation patterns analogous to that for Pu(IV) oxide (i.e., PuO_2).[20-21] However, the structural disorder in the oxyhydroxide compounds causes the diminution of EXAFS

amplitude as compared with the amplitude for the structurally well-ordered PuO_2, finally reducing the magnitude of EXAFS-FT peaks.[20] The EXAFS spectra in Figure S15 exhibit exactly the same trend. That is, the Pu particle shows an EXAFS oscillation pattern similar to that for PuO_2(s) (Figure S15-left), whilst its EXAFS amplitude (Figure S15-left) and the peak magnitude in the corresponding EXAFS-FT (Figure S15-right) are obviously smaller than those for PuO_2(s). (Note that in Figure S15, the EXAFS amplitude and FT magnitude for the particle are multiplied by four for a better spectral comparison with the PuO_2(s) data.) This indicates that the local structural arrangement of Pu in the particle would be similar to that in PuO_2, but significantly disordered as observed in the oxyhydroxide system (i.e., $PuO_{2+x-y}(OH)_{2y}\cdot zH_2O$)[20] or poorly structured in the long-range order.

The oxyhydroxide compounds of Pu can be produced through the oxidation of metallic Pu at high temperature,[16] which is a possible scenario during the initial detonation-explosion process of the Pu fuel component. The EXAFS structural parameters in Table S1 suggest that the Pu–O and Pu–Pu interatomic distances (*R*) obtained for the Pu particle are comparable to those for PuO_2(s) or $PuO_{2+x-y}(OH)_{2y}\cdot zH_2O$[20] but they are obviously different from those for lower Pu oxides (i.e., PuO and Pu_2O_3), which is consistent with the above discussions.

The Pu–O distance in the Pu particle (2.28 ± 0.02 Å) is significantly shorter than that for PuO_2(s) (2.33 Å) or for $PuO_{2+x-y}(OH)_{2y}\cdot zH_2O$[20] (2.46~2.62 Å on average). This potentially suggests the partial oxidation of Pu(IV) to higher oxidation states (i.e., Pu(V) or –(VI)) in the PuO_2-based matrix[22] or similar. Given the fact that TNT was reportedly employed as a chemical explosive in "*Minor Trials*" at the Taranaki test site (e.g., the operation "*Vixen B*"),[23] the temperature during the detonation-explosion process is expected to rise up to > 3,000 ^{o}C.[24] Such an extremely high temperature could induce the partial oxidation of Pu to higher than tetravalent, potentially resulting in the formation of poorly structured oxyhydroxide compounds. This could account for the observed shortening of Pu–O distance and lower coordination numbers of Pu–O and Pu–Pu shells in the particle (Table S1).

Based on the XANES and EXAFS results discussed above, the Pu in the isolated particle could be characterised as a poorly structured form of oxyhydroxide compounds. The oxidation state of Pu in the particle is primarily tetravalent (Pu(IV)) possibly with partial oxidation to higher valences.

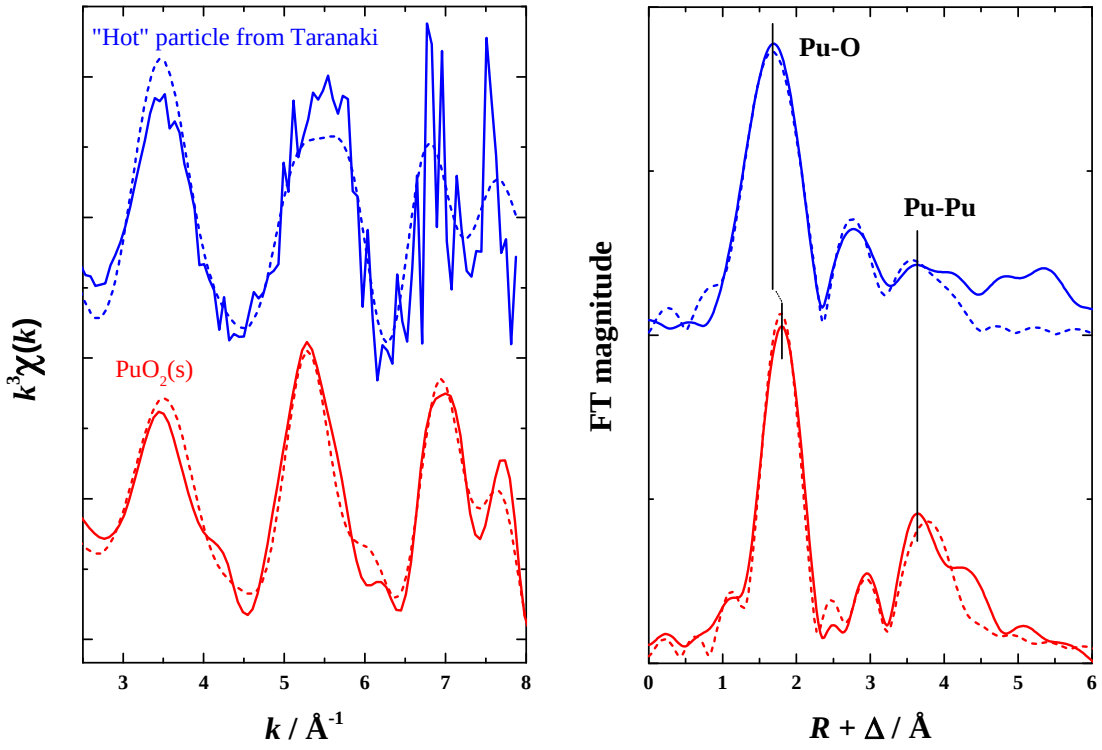

Figure S15. k^3-weighted Pu L_{III}-edge EXAFS spectra for the particle and PuO_2(s)[17] (left) and their corresponding Fourier transforms (right). Solid lines; experimental data, dotted lines; theoretical fitting. *k*-range for Fourier transform; k = 2.50 – 7.75 Å^{-1}. The EXAFS amplitude and FT magnitude for the particle (i.e., blue data) are multiplied by four for a better spectral comparison with the PuO_2(s) data. Phase shifts (Δ) are not corrected on the Fourier transforms. The data for PuO_2(s) was provided through the courtesy of P. M. Martin (CEA-Cadarache).

Table S1. Summary of EXAFS metrical parameters obtained from theoretical curve fitting

	Pu-O[a]			Pu-Pu[b]						
	CN[c]	*R* / Å[d]	σ^2 / Å^{2e}	*CN*[c]	*R* / Å[d]	σ^2 / Å^{2e}	ΔE_0 / eV[f]	S_0^2 (fixed)	χ^{2g}	*R*-factor / %[g]
"Hot" particle from Maralinga	4.7	2.28	0.020	2.9	3.88	0.015	-0.05	0.9	45738	14.2
PuO_2(s)	8[h]	2.33	0.004	12[h]	3.82	0.005	3.31	0.9	1172974	15.9
PuO_2(s) - crystal structure[i]	8	2.337		12	3.817					
Pu_2O_3(s) - crystal structure[j]	7	2.464		12	3.768					
PuO(s) - crystal structure[k]	6	2.480		12	3.507					

[a,b] Single scattering shells. [c] Coordination numbers; error = *CN* ± 25%. [d] Interatomic distances; error = *R* ± 0.02 Å. [e] Debye-Waller factors; error = σ^2 ± 0.002 Å^2. [f] Shifts in threshold energy (ΔE_0) were variable but constrained to be the same value for all the scattering shells during fitting; error = ΔE_0 ± 0.05 eV. [g] Measures of goodness of fitting recommended by the International X-ray Absorption Society [25]. [h] Fixed values. [i] Reference [26]. [j] Reference [27]. [k] Reference [28].

Morphology of the isolated Pu particle

Given that the series of the sample fragments was obtained from the single particle (*i.e.*, identical origin), the elemental distributions shown in Figures S6-S10 and Figure 2 in the main text can be interpreted as a fragmented Pu particle that has an external layer containing Ca/Fe/U, as modelled in Figure S16. That is, the particle core is primarily composed of a pure phase of a Pu compound, whilst the outer surface of the particle is covered by Ca/Fe/U layers. This can be visualised more clearly when we perform the image analysis on the acquired XFM images. For instance, the result of image analysis on the images of the fragment **3** (Fig. S8 = Fig. 2 in the main text) reveals that Pu and Pb are rather localised inside the fragment (*i.e.*, particle core), whilst Ca and Fe are detected primarily at the edge of the fragment (*i.e.*, external layer) (Fig. S17). On the other hand, all the detected elements are distributed more evenly on the fragment **2** in Fig. S7, which is assumed to be a view of the particle surface from outside (Fig. S18). Assuming this "*core shell*" structure, the fragment images in Figures S7 and S8 appear to be cross sections of the original particle (the lower left and middle illustrations in Figure S16), whilst Figures S6, S9 and S10 depict a view of the particle surface from outside (the upper right illustration in Figure S16). As shown in Figure S2, the Pu phase in the isolated particle was consistent with unfissioned Pu material originating from a weapons component. The Ca, Fe and U forming the surface layer are likely to originate from the local soils, which are reported to be rich in these elements.[29]

The distribution of Pb appears to be similar to that of Pu, which suggests that Pb is an intrinsic component of the particle core and not from the natural accumulation after the detonation. Pb isotopes were also detected in the post-detonation debris, "Trinitite", from the Pu-based nuclear bomb test at New Mexico, USA, in 1945 [30]. These Pb isotopes in "Trinitite" are attributed to the tamper material of the original nuclear bomb assembly, which is often composed of either Pb-metal/alloy or U-metal.[3] The first of these directly contributes to the presence of Pb isotopes in the debris, whilst the latter produces Pb isotopes as a decay product of ^{235}U in the U material.[30] Our gamma measurement in Figure S1 indicates no significant contribution of radioactive Pb isotopes in the particle. Additionally, a considerable amount of Pb was also used as a radiation shielding material and/or as a construction material of the firing devices for "*Minor Trials*" at Maralinga.[1] Therefore, Pb in the particle probably originates either in the Pb-metal/alloy tamper or in the shielding/construction materials of the firing devices.

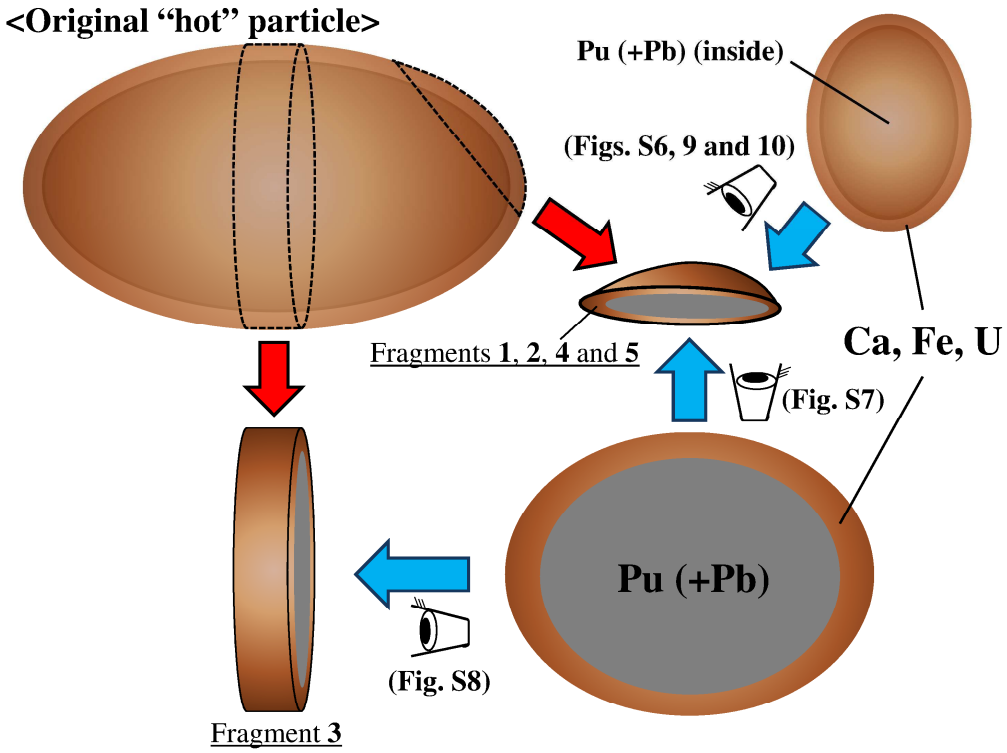

Figure S16. Illustration of the "core shell" model being composed of the Pu+Pb core coated with a Ca/Fe/U outer layer and possible two-dimensional visions of fragments from different points of view.

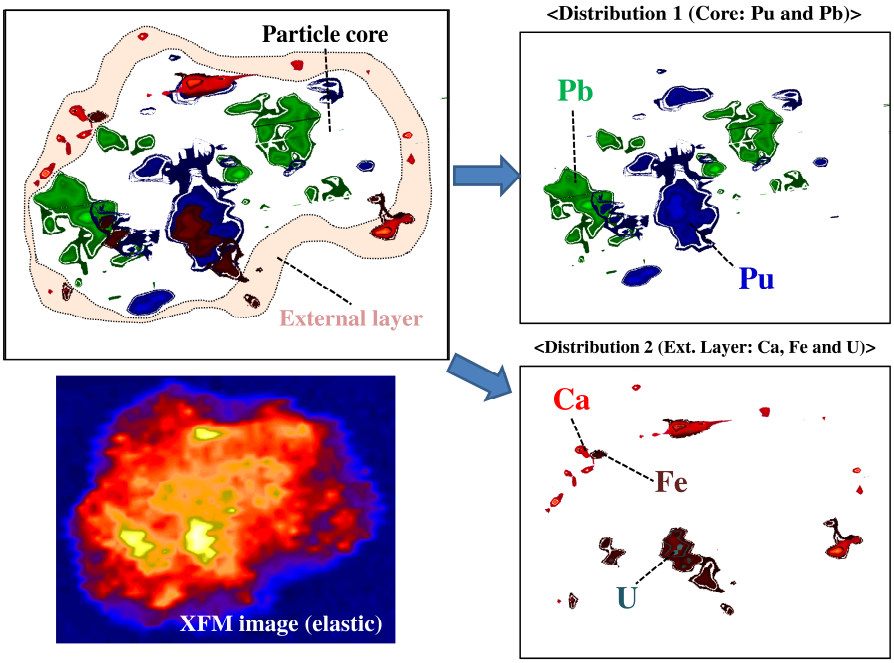

Figure S17. Results of image analysis on the XFM images in Fig. S8 for the fragment **3**.

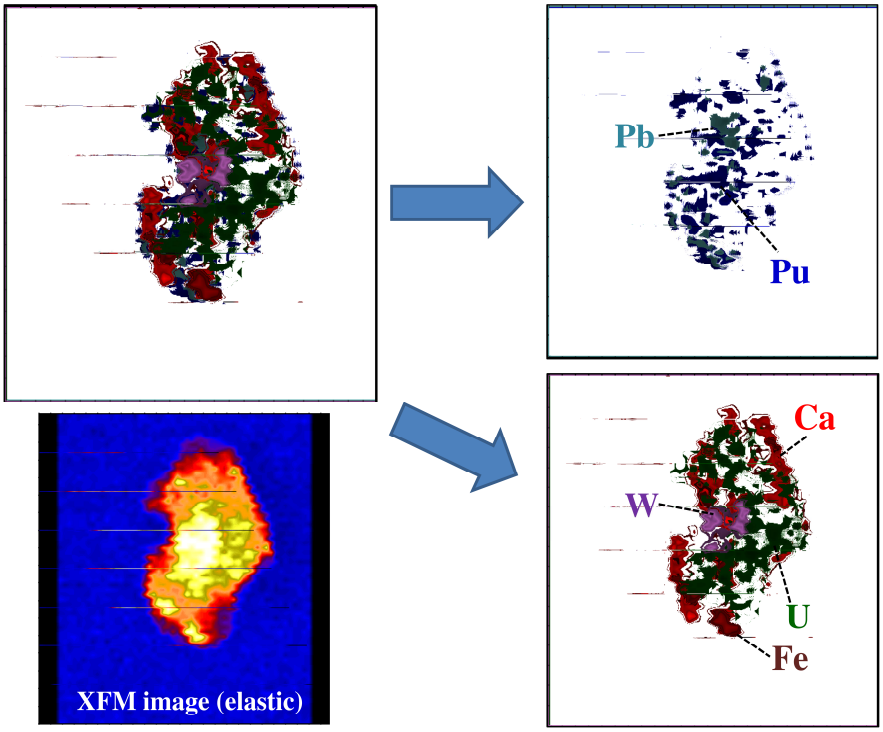

Figure S18. Results of image analysis on the XFM images in Fig. S7 for the fragment **2**.

References

1. The Maralinga Rehabilitation Technical Advisory Committee, *Rehabilitation of former nuclear test sites at Emu and Maralinga (Australia) 2003*; 0642-77328-9; The Maralinga Rehabilitation Technical Advisory Committee: Canberra, Australia, 2003.
2. Johansen, M. P.; Child, D. P.; Caffrey, E. A.; Davis, E.; Harrison, J. J.; Hotchkis, M. A. C.; Payne, T. E.; Ikeda-Ohno, A.; Thiruvoth, S.; Twining, J. R.; Beresford, N. A., Accumulation of plutonium in mammalian wildlife tissues following dispersal by accidental-release tests. *J. Environ. Radioactiv.* **2016,** *151* (2), 387-394.
3. Norris, R. S.; Burrows, A. S.; Fieldhouse, R. W., *Britisch, French, and Chinese nuclear weapons*. Westview Press: 1994; Vol. V.
4. Paterson, D.; de Jonge, M. D.; Howard, D. L.; Lewis, W.; McKinlay, J.; Starritt, A.; Kusel, M.; Ryan, C. G.; Kirkham, R.; Moorhead, G.; Siddons, D. P.; McNulty, I.; Eyberger, C.; Lai, B., The X-ray Fluorescence Microscopy Beamline at the Australian Synchrotron. *AIP Conf. Proc.* **2011,** *1365* (219), 219-222.
5. Howard, D. L.; de Jonge, M. D.; Lau, D.; Hay, D.; Varcoe-Cocks, M.; Ryan, C. G.; Kirkham, R.; Moorhead, G.; Paterson, D.; Thurrowgood, D., High-definition X-ray fluorescence elemental mapping of paintings. *Anal. Chem.* **2012,** *84* (7), 3278-3286.
6. Etschmann, B. E.; Ryan, C. G.; Brugger, J.; Kirkham, R.; Hough, R. M.; Moorhead, G.; Siddons, D. P.; De Geronimo, G.; Kuczewski, A.; Dunn, P.; Paterson, D.; De Jonge, M. D.; Howard, D. L.; Davey, P.; Jensen, M., Reduced As components in highly oxidized

environments: Evidence from full spectral XANES imaging using the Maia massively parallel detector. *Amer. Mineralog.* **2010,** *95* (5-6), 884-887.
7. Ryan, C. G.; Siddons, D. P.; Kirkham, R.; Li, Z. Y.; de Jonge, M. D.; Paterson, D. J.; Kuczewski, A.; Howard, D. L.; Dunn, P. A.; Falkenberg, G.; Boesenberg, U.; De Geronimo, G.; Fisher, L. A.; Halfpenny, A.; Lintern, M. J.; Lombi, E.; Dyl, K. A.; Jensen, M.; Moorhead, G. F.; Cleverley, J. S.; Hough, R. M.; Godel, B.; Barnes, S. J.; James, S. A.; Spiers, K. M.; Alfeld, M.; Wellenreuther, G.; Vukmanovic, Z.; Borg, S., Maia X-ray fluorescence imaging: Capturing detail in complex natural samples. *J. Phys.: Conf. Ser.* **2014,** *499*, 012002.
8. Ryan, C. G.; Cousens, D. R.; Sie, S. H.; Griffin, W. L.; Suter, G. F., Quantitative PIXE microanalysis of geological material using the CSIRO proton microprobe. *Nucl. Inst. Methods Phys. Res. B* **1990,** *47* (1), 55-71.
9. Ressler, T., WinXAS: a program for X-ray absorption spectroscopy data analysis under MS-Windows. *J. Synchrotron Radiat.* **1998,** *5* (2), 118-122.
10. Ryan, C. G., Quantitative trace element imaging using PIXE and the nuclear microprobe. *Int. J. Imaging Syst. Technol.* **2000,** *11* (4), 219-230.
11. Prins, R.; Koningsberger, D. E., *X-ray absorption: Principles, applications, techniques for EXAFS, SEXAFS, and XANES*. Wiley Interscience: New York, 1988.
12. Ankudinov, A. L.; Ravel, B.; Rehr, J. J.; Conradson, S. D., Real-space multiple-scattering calculation and interpretation of x-ray-absorption near-edge structure. *Phys. Rev. B* **1998,** *58* (12), 7565-7576.
13. Wyckoff, R. W. G., *Cryst. Struct.* **1963,** *1*, 7-83, 239-444.
14. Matz, W.; Schell, N.; Bernhard, G.; Prokert, F.; Reich, T.; Claussner, J.; Oehme, W.; Schlenk, R.; Dienel, S.; Funke, H.; Eichhorn, F.; Betzl, M.; Prohl, D.; Strauch, S.; Huttig, G.; Krug, H.; Neumann, W.; Brendler, V.; Reichel, P.; Denecke, M. A.; Nitsche, H., ROBL - a CRG beamline for radiochemistry and materials research at the ESRF. *J. Synchrotron Rad.* **1999,** *6* (6), 1076-1085.
15. http://henke.lbl.gov/optical_constants/atten2.html.
16. Conradson, S. D.; Abney, J. D.; Begg, B. D.; Brady, E. D.; Clark, D. L.; den Auwer, C.; Ding, M.; Dorhout, P. K.; Espinosa-Faller, F. J.; Gordon, P. L.; Haire, R. G.; Hess, N. J.; Hess, R. F.; Keogh, D. W.; Lander, G. H.; Lupinetti, A. J.; Morales, L. A.; Neu, M. P.; Palmer, P. D.; Paviet-Hartmann, P.; Reilly, S. D.; Runde, W. H.; Tait, C. D.; Veirs, D. K.; Wastin, F., Higher order speciation effects on plutonium L_3 X-ray absorption near nedge spectra. *Inorg. Chem.* **2004,** *43* (1), 116-131.
17. Martin, P.; Grandjean, S.; Valot, C.; Carlot, G.; Ripert, M.; Blanc, P.; Hennig, C., XAS study of $(U_{1-y}Pu_y)O_2$ solid solutions. *J. Alloys Compd.* **2007,** *444-445*, 410-414.
18. Haschke, J. M.; Allen, T. H.; Morales, L. A., Surface and corrosion chemistry of plutonium. *Los Alamos Science* **2000,** *26*, 252-273.
19. Clark, D. L.; Hecker, S. S.; Jarvinen, G. D.; Neu, M. P., Plutonium. In *The Chemistry of the Actinide and Transactinide Elements*, Third edition ed.; Morss, L. R.; Edelstein, N. M.; Fuger, J.; Katz, J. J., Eds. Springer: Dordrecht, The Netherland, 2006; Vol. 2, pp 1028-1036.
20. Conradson, S. D.; Begg, B. D.; Clark, D. L.; Den Auwer, C.; Ding, M.; Dorhout, P. K.; Espinosa-Faller, F. J.; Gordon, P. L.; Haire, R. G.; Hess, N. J.; Hess, R. F.; Keogh, D. W.; Morales, L. A.; Neu, M. P.; Paviet-Hartmann, P.; Runde, W. H.; Tait, C. D.; Veirs, D. K.; Villella, P. M., Local and nanoscale structure and speciation in the $PuO_{2+x-y}(OH)_{2y}\cdot z(H_2O)$ system. *J. Am. Chem. Soc.* **2004,** *126* (41), 13443-13458.
21. Rothe, J.; Walther, C.; Denecke, M. A.; Fanghanel, T., XAFS and LIBD investigation of the formation and structure of colloidal Pu(IV) hydrolysis products. *Inorg. Chem.* **2004,** *43* (15), 4708-4718.
22. Haschke, J. M.; Allen, T. H.; Morales, L. A., Reaction of plutonium dioxide with water: Formation and properties of PuO_{2+x}. *Science* **2000,** *287* (5451), 285-287.
23. Tynan, L., Dig for secrets: the lesson of Maralinga's Vixen B. *Chain React.* **2013,** (119), 42.
24. Danilenko, V. V., Nanocarbon phase diagram and conditions for detonation nanodiamond formation. In *Synthesis, Properties and Applications of Ultrananocrystalline Diamond* -

NATO Science Series II, Gruen, D. M.; Shenderova, O. A.; Ya. Vul', A., Eds. Springer: Dordrecht, The Netherland, 2005; Vol. 192, pp 181-198.
25. *Error Reporting Recommendations: A Report of the Standard and Criteria Committee*; International X-ray Absorption Society: July 26, 2000, 2000.
26. Belin, R. C.; Valenza, P. J.; Reynaud, M. A.; Raison, P. E., New hermetic sample holder for radioactive materials fitting to Siemens D5000 and Bruker D8 X-ray diffractometers: application to the Rietveld analysis of plutonium dioxide. *J. Appl. Crystallogr.* **2004,** *37* (6), 1034-1037.
27. Wulff, M.; Lander, G. H., Magnetic structure and Pu ground state in β-Pu_2O_3. *J. Chem. Phys.* **1988,** *89* (5), 3295-3299.
28. Chikalla, T. D.; McNeilly, C. E.; Skavdahl, R. E., The plutonium-oxygen system. *J. Nucl. Mater.* **1964,** *12* (2), 131-141.
29. Cooper, M. B.; Burns, P. A.; Tracy, B. L.; Wilks, M. J.; Williams, G. A., Characterization of plutonium contamination at the former nuclear weapons testing range at Maralinga in South Australia. *J. Radioanal. Nucl. Chem.* **1994,** *177* (1), 161-184.
30. Fahey, A. J.; Zeissler, C. J.; Newbury, D. E.; Davis, J.; Lindstrom, R. M., Postdetonation nuclear debris for attribution. *Proc. Natl. Acad. Sci. USA* **2010,** *107* (47), 20207-20212.